Characterization of non-Gaussian conductivities and porosities with hydraulic heads, solute concentrations and water temperatures

Teng Xu,[1] and J. Jaime Gómez-Hernández[1]

Corresponding author: Teng Xu, Institute for Water and Environmental Engineering, Universitat Politècnica de València, Camino de Vera, s/n, 46022 Valencia, Spain. (tenxu@posgrado.upv.es)

[1]Institute for Water and Environmental Engineering, Universitat Politècnica de València, Valencia, Spain.

Abstract.

Reliable characterization of hydraulic parameters is important for the understanding of groundwater flow and solute transport. The normal-score ensemble Kalman filter (NS-EnKF) has proven to be an effective inverse method for the characterization of non-Gaussian hydraulic conductivities by assimilating transient piezometric head data, or solute concentration data. Groundwater temperature, an easily captured state variable, has not drawn much attention as an additional state variable useful for the characterization of aquifer parameters. In this work, we jointly estimate non-Gaussian aquifer parameters (hydraulic conductivities and porosities) by assimilating three kinds of state variables (piezometric head, solute concentration, and groundwater temperature) using the NS-EnKF. A synthetic example including seven tests is designed, and used to evaluate the ability to characterize hydraulic conductivity and porosity in a non-Gaussian setting by assimilating different numbers and types of state variables. The results show that characterization of aquifer parameters can be improved by assimilating groundwater temperature data and that the main patters of the non-Gaussian reference fields can be retrieved with more accuracy and higher precision if multiple state variables are assimilated.

1. Introduction

Reliable characterization of hydraulic parameters is important for the understanding of groundwater flow and solute transport [*Gómez-Hernández and Wen*, 1994; *Gómez-Hernández et al.*, 2003]. However, in reality, due to practical reasons, the information we can get is sparse, what makes direct characterization difficult [*Zhou et al.*, 2014]. Better characterization can be achieved by stochastic inverse modeling, making use of observed data of state variables.

In the last decades, many works have focused on the inverse characterization of hydraulic parameters by assimilating piezometric heads. Less attention has been paid on the joint assimilation of two or more types of state variables; *Franssen et al.* [2003] presented an extension of the self-calibrating method [*Wen et al.*, 1999] and showed the importance, for aquifer characterization and flow predictions, of conditioning on piezometric head and concentration data; *Li et al.* [2012a] jointly characterized hydraulic conductivity and porosity by the simultaneous assimilation of piezometric heads and solute concentration using the ensemble Kalman Filter (EnKF); *Fu and Gómez-Hernández* [2009] analyzed the characterization of aquifer conductivities by conditioning on piezometric head data as well as on solute travel time data via a blocking Markov chain Monte Carlo method.

Recently, groundwater temperature data are attracting attention thanks to the wide use of inexpensive temperature loggers. Groundwater temperature data and heat transport modeling could be used in inverse modeling together with head and solute transport data, [e.g., *Anderson*, 2005; *Ma and Zheng*, 2010]. Groundwater temperature can provide additional information on aquifer structure, especially about the connectivity patterns within an aquifer [*Kurtz et al.*, 2014]. There are already works demonstrating the benefits of the joint assimilation of temperature data and other state variables, particularly in the analysis of surface water-groundwater interaction. For example, *Doussan et al.* [1994] characterized river-groundwater exchanges by the coupled use of hydraulic heads and temperature data in a river-aquifer system; *Bravo et al.* [2002] estimated simultaneously hydraulic conductivities and inflow to wetland systems by the joint inversion of head and temperature data with PEST [*Doherty et al.*, 1994]; and *Kurtz et al.* [2014] characterized hydraulic conductivities and leakage coefficients by the assimilation of piezometric heads and groundwater temperatures in a river-aquifer system using the EnKF.

However, except for works in the analysis of surface water-groundwater interactions, groundwater temperature is seldom used for aquifer characterization. We want to show the importance of the use of temperature data, together with other state variables for the characterization of non-Gaussian hydraulic conductivities in inverse modeling using the EnKF.

In the last decades, many inverse modeling methods have been developed and successfully applied for hydraulic conductivity characterization, such as the gradual deformation method, the sequential self calibration, the Markov chain Monte Carlo method, the Representer method, the Pilot Points method, the particle filter, the inverse sequential simulation method and the EnKF [e.g., *Capilla and Llopis-Albert*, 2009; *Hu*, 2000; *Gómez-Hernánez et al.*, 1997; *Fu and Gómez-Hernández*, 2009; *Oliver et al.*, 1997; *Alcolea et al.*, 2006; *Wen et al.*, 2002; *RamaRao et al.*, 1995; *Franssen et al.*, 2003; *Gordon et al.*, 1993; *Losa et al.*, 2003; *Van Leeuwen*, 2009; *Xu and Gómez-Hernández*, 2015a, b; *Evensen*, 2003; *Gu and Oliver*, 2006; *Wen and Chen*, 2006]. Of all of them, the EnKF has proven to be the most computationally efficient and capable to handle non-Gaussianities and non-linearities between parameters and state variables.

The EnKF is developed after the Kalman filter [*Kalman et al.*, 1960], overcoming the problem associated with the estimation of the non-stationary auto-covariances and cross-covariances of parameters and state variables associated with non-linear state-transfer functions. However, in its original implementation [*Evensen*, 2003], the EnKF fails to properly characterize parameters following a non-Gaussian distribution. Several approaches have been developed for the EnKF to deal with parameters following non-Gaussian distributions. *Xu et al.* [2013] has grouped these approaches into four categories according to their characteristics: (i) Combination of the EnKF with a Gaussian mixture model [e.g., *Sun et al.*, 2009; *Dovera and Della Rossa*, 2011; *Reich*, 2011], (ii) reparameterization of the EnKF formulation [e.g., *Chen et al.*, 2009; *Chen and Oliver*, 2010; *Chang et al.*, 2010], (iii) iterative EnKF [e.g., *Liu and Oliver*, 2005; *Gu and Oliver*, 2007; *Wang et al.*, 2010], and (iv) combination of the EnKF with a normal-score (NS) transform [e.g., *Simon and Bertino*, 2009; *Zhou et al.*, 2011; *Li et al.*, 2012b].

In this paper, we analyze how well non-Gaussian hydraulic conductivity and porosity fields can be characterizated by the joint assimilation of piezometric heads, solute concentration and groundwater temperature data using the normal-score Ensemble Kalman Filter (NS-EnKF) as proposed by *Zhou et al.* [2011]. The paper starts with a description of the algorithms, and then we evaluate its performance in seven synthetic scenarios. The paper ends with a discussion and a summary.

2. Methodology

The NS-EnKF is applied for the characterization of a non-Gaussian conductivity field and a non-Gaussian porosity field by the sequential assimilation in time of piezometric head, solute concentration, and groundwater temperature data. There are three state variables of interest, and three state equations, which are modeled in transient conditions with the corresponding numerical codes.

2.1. Transient groundwater flow

Piezometric heads evolve in time according to the following three-dimensional transient groundwater flow equation with external sources/sinks [*Bear*, 1972]:

$$S_s \frac{\partial H}{\partial t} - \nabla \cdot (K \nabla H) = W \tag{1}$$

where $\nabla\cdot$ is the divergence operator, ∇ is the gradient operator, S_s denotes specific storage (L^{-1}), H is the hydraulic head (L), K is the hydraulic conductivity (LT^{-1}), W denotes sources and sinks per unit volume (T^{-1}), and t is time (T).

This equation is numerically solved, given initial and boundary conditions, by finite differences using the MODFLOW code [*McDonald and Harbaugh*, 1988], and the resulting specific discharges ($\mathbf{q} = -K\nabla H$) are used as input to the solute and heat transport equations presented next.

2.2. Solute transport

Solute concentrations evolve in time according to the following three-dimensional transport equation [*Zheng*, 2010]:

$$(1 + \frac{\rho_b}{\theta} k_d) \frac{\partial(\theta C)}{\partial t} = \nabla \cdot [\theta(D_m + \alpha \frac{\mathbf{q}}{\theta}) \cdot \nabla C] - \nabla \cdot (\mathbf{q} C) - q_s C_s \tag{2}$$

where θ is the effective porosity (dimensionless), ρ_b (ML^{-3}) is the the bulk density of the rock matrix($\rho_b = \rho_s(1-\theta)$, where ρ_s (ML^{-3}) is the density of the solid grains), k_d is the distribution coefficient (L^{3}M^{-1}), C is the aqueous concentration (ML^{-3}), t is time (T), D_m is the molecular diffusion coefficient (L^{2}T^{-1}), α is the dispersivity tensor (L), $\mathbf{q}$ is the specific discharge vector related to the hydraulic head through, $\mathbf{q} = (-K\nabla H)$ (LT^{-1}), q_s is the volumetric flow rate per unit volume representing fluid sources or sinks (T^{-1}), and C_s is the concentration of the source or sink flux (ML^{-3}).

This equation is numerically solved, given initial and boundary conditions, by the MT3DMS code [e.g., *Zheng*, 2010; *Ma et al.*, 2012].

2.3. Heat Transport

Groundwater temperatures evolve in time due to heat convection with the fluid phase, heat conduction and dispersion through the fluid and aquifer sediment, and heat exchange between the aqueous phase and the aquifer sediment. The state equation is the following [e.g., *Healy and Ronan*, 1996; *Anderson*, 2005]:

$$(1 + \frac{1-\theta}{\theta} \frac{\rho_s}{\rho_w} \frac{c_s}{c_w}) \frac{\partial(\theta T)}{\partial t} = \nabla \cdot [\theta(\frac{\theta k_w + (1-\theta) k_s}{\theta \rho_w c_w} + \alpha \frac{\mathbf{q}}{\theta}) \cdot \nabla T] - \nabla \cdot (\mathbf{q} T) + q_s T_s \tag{3}$$

where c_s is the specific heat capacity of the solid (L^{2}T$^{-2}\Theta^{-1}$), ρ_w is the density of the fluid (ML^{-3}), c_w is the specific heat capacity of the fluid (L^{2}T$^{-2}\Theta^{-1}$), T is the fluid temperature (Θ), k_s and k_w are the thermal conductivities of the solid and fluid phase, respectively (MLΘ^{-1}T^{-3}); and T_s is the source/sink temperature (Θ).

Comparing Eq. (3) and Eq. (2), we can find great similarity between them. Indeed, replacing $c_s/c_w\rho_w$ in Eq. (3) with a fictitious distribution coefficient, and $(\theta k_w + (1-\theta)k_s)/\theta\rho_w c_w$ with a fictitious molecular diffusion, and assuming that the changes in temperature are small and do not affect fluid density; Eq. (3) becomes Eq. (2). Therefore, the same MT3DMS code used for solute transport modeling can be used for the modeling of heat transport [e.g., *Zheng*, 2010; *Ma et al.*, 2012; *Ma and Zheng*, 2010].

2.4. Modeling process

Modeling is performed in transient conditions. First, the groundwater flow equation is solved to predict the piezometric heads in the next time step. The flow solution is used to compute the specific discharges that are needed for the solution of the solute and heat transport equations. Then, these two equations are solved, independently of each other, to advance the prediction of concentrations and temperatures to the next time step.

2.5. Normal-score ensemble Kalman filter

Next, we present a generalized version of the NS-EnKF [e.g., *Zhou et al.*, 2012; *Li et al.*, 2012c; *Xu et al.*, 2013] for the characterization of l kinds of non-Gaussian parameters $(P_1, P_2, ..., P_l)$ with the assimilation of m types of state variables $(V_1, V_2, ..., V_m)$:

1. Initialization step. Ensembles of all the parameters $(P_1, P_2, ..., P_l)$ are generated. In the examples analyzed next, the generation of the non-Gaussian fields consists of two steps: in the first step, facies realizations are generated, and then, these realizations are populated with parameter values according to distributions specific for each facies and parameter.

2. Normal-score transform step. At each location, all parameter values of all realizations for each hydraulic parameter are transformed into normal scores using specific transform functions at each location and for each parameter:

$$\tilde{P}_i = \phi_i(P_i), \quad i = 1, \ldots, l. \tag{4}$$

where ϕ_i is a vectorial normal-score transform function for the i^{th} hydraulic parameter, which varies from one location to another.

3. Forecasting step. State variables at time step t are calculated based on the state variables at time step $t-1$ and the last estimate of the parameter fields, using the corresponding numerical codes. As already mentioned, we use MODFLOW to solve the three dimensional transient groundwater flow equation, and MT3DMS to solve the solute transport equation and the heat transport equation.

$$V_j^t = \psi_j(V_j^{t-1}, P_1^{t-1}, P_2^{t-1}, ..., P_l^{t-1}), \quad j = 1, \ldots, m. \tag{5}$$

where ψ_j is the j^{th} state variable forecasting model.

This forecast is performed for each ensemble member.

4. Assimilation step. An augmented state vector S including transformed parameters and variables is built and then updated on the basis of the discrepancies between forecast states and observed state measurements:

$$S = \begin{pmatrix} V_1 \\ V_2 \\ \dots \\ V_m \\ \tilde{P}_1 \\ \tilde{P}_2 \\ \dots \\ \tilde{P}_l \end{pmatrix} \tag{6}$$

such a vector is built for each member of the ensemble, and it is updated (for each ensemble member) according to

$$S_t^a = S_t^f + G_t[V_t^o + e_t - \hat{V}] \tag{7}$$

with

$$G_t = F_t H^T (H F_t H^T + R_t)^{-1} \tag{8}$$

where S_t^a is the updated state vector at the t^{th} time step; S_t^f is the forecasted state vector at the t^{th} time step; G_t is the Kalman gain; e_t is an observation error with zero mean and covariance R_t; V_t^o represents the observed values of the state variables, while $\hat{V}$ are the state variables at the observation locations as computed from the model forecast; F_t is the augmented state covariance matrix, and H is a measurement matrix used to map forecasted values at the discretization nodes onto the observation locations. When observation locations coincide with the model nodes, this matrix contains only $0's$ and $1's$, and Eq. (8) can be rewritten as:

$$G_t = C_{\widetilde{S}\hat{V}} (C_{\hat{V}\hat{V}} + R_t)^{-1} \tag{9}$$

where $C_{\widetilde{S}\hat{V}}$ is the cross-covariance between the augmented state vector and the state variables at the observation locations; $C_{\hat{V}\hat{V}}$ is the covariance between state variables at observation locations. These covariances are non-stationary and are computed from the members of the ensemble; they are computed only once at each time step.

If, these covariances are split into the auto- and cross-covariances of each of the l parameters and m state variables, and we define $d = V^0 + e - \hat{V}$ and $D_{\hat{V}\hat{V}} = \left(C_{\hat{V}\hat{V}} + R_t\right)^{-1}$, the updating equation (7) becomes:

$$S^a = \begin{pmatrix} V_1 \\ V_2 \\ \cdots \\ V_m \\ \tilde{P}_1 \\ \tilde{P}_2 \\ \cdots \\ \tilde{P}_l \end{pmatrix} + \begin{pmatrix} C_{V_1\hat{V}_1} & C_{V_1\hat{V}_2} & \cdots & C_{V_1\hat{V}_m} \\ C_{V_2\hat{V}_1} & C_{V_2\hat{V}_2} & \cdots & C_{V_2\hat{V}_m} \\ \cdots & \cdots & \cdots & \cdots \\ C_{V_m\hat{V}_1} & C_{V_m\hat{V}_2} & \cdots & C_{V_m\hat{V}_m} \\ C_{\tilde{P}_1\hat{V}_1} & C_{\tilde{P}_1\hat{V}_2} & \cdots & C_{\tilde{P}_1\hat{V}_m} \\ C_{\tilde{P}_2\hat{V}_1} & C_{\tilde{P}_2\hat{V}_2} & \cdots & C_{\tilde{P}_2\hat{V}_m} \\ \cdots & \cdots & \cdots & \cdots \\ C_{\tilde{P}_l\hat{V}_1} & C_{\tilde{P}_l\hat{V}_2} & \cdots & C_{\tilde{P}_l\hat{V}_m} \end{pmatrix} \begin{pmatrix} D_{\hat{V}_1\hat{V}_1} & D_{\hat{V}_1\hat{V}_2} & \cdots & D_{\hat{V}_1\hat{V}_m} \\ D_{\hat{V}_2\hat{V}_1} & D_{\hat{V}_2\hat{V}_2} & \cdots & D_{\hat{V}_2\hat{V}_m} \\ \cdots & \cdots & \cdots & \cdots \\ D_{\hat{V}_m\hat{V}_1} & D_{\hat{V}_m\hat{V}_2} & \cdots & D_{\hat{V}_m\hat{V}_m} \end{pmatrix} \begin{pmatrix} d_1 \\ d_2 \\ \cdots \\ d_m \end{pmatrix} \tag{10}$$

where all the auto- and cross-covariances between the different components of the augmented vector are explicitly shown. Recall that this updating is performed for each ensemble member, where only the vector with the d values changes from one ensemble member to another.

As already mentioned, the covariances in (10) are computed from the ensemble of realizations. When the ensemble size is small, chances are that spurious correlations may appear between variables at long distances, or that covariances are repeatedly underestimated with the risk of collapsing to zero into what is referred to as ensemble in-breeding. These two problems are addressed with the use of covariance localization and inflation [*Xu et al.*, 2013]. In the present example, with an ensemble size of 600 members, it was not necessary to use neither localization nor inflation. The application of either technique to a multivariate case should not be much different than when dealing with a single parameter: each of the covariances matrices should be localized to avoid the existence of non-zero correlations at long distances; the same localization function could be used for all the covariances, or they could be different, with the only caution of not forcing too small covariances at distances for which correlation is expected (this step can be supervised by plotting some of the experimental covariances to determine the distance at which the spurious values appear); similarly, each covariance should be inflated, and the inflation could be computed for each variable using the standard algorithms for that purpose.

5. Back transformation step. All the updated normal scores of the parameters of all ensemble members are transformed back into parameter space using the inverse of the previously used transform functions:

$$P_i = \phi_i^{-1}(\tilde{P}_i), \quad i = 1, \ldots, l. \tag{11}$$

6. Return to step 3 and repeat the processes until all the observed data are assimilated.

3. Synthetic Example

A synthetic channelized confined aquifer of size 50 m by 50 m by 5 m is constructed and discretized into 50 by 50 by 1 cells. The channels represent 35% of the aquifer and contain high permeability-intermediate porosity material, whereas the 65% non-channel material is of low permeability and high porosity. The aquifer is constructed in two steps; in the first step a binary facies realization is generated using the SNESIM code (*Strebelle* [2002]) with the training image in Figure 1 and with eight conditioning facies data shown in Figure 2. Then, the GCOSIM3D code (*Gómez-Hernández and Journel* [1993]) is used to populate each facies, independently, with $\ln K$ and porosity values drawn from multiGaussian distributions with the parameters given in Table 1. In our example, both parameters are generated independently; however, they could be cross-correlated, and such a cross-correlation should be taken into account here. Later on, during the updating process, the ensemble cross-correlation between the parameters will be accounted for in the calculation of the covariances needed to determine the Kalman gain.

The resulting reference fields of $\ln K$ and porosity and their histograms are shown in Figure 3 and Figure 4, respectively. Globally, both $\ln K$ and porosity follow clearly non-Gaussian models, with a mean of -0.3 ln(m/d), and a standard deviation of 3.1 ln(m/d) for $\ln K$, and a mean of 0.3, and a standard deviation of 0.1 for porosity. All other parameters needed for the modeling of groundwater and solute and heat transport are considered homogeneous and uniform throughout the entire aquifer, with values that are described next.

All four boundaries of the aquifer are impermeable to flow and solute and heat transport. Specific storage is set to 0.03 m^{-1}. (Strictly speaking, we should have used a heterogeneous specific storage strongly correlated with the porosity; however, such a consideration implied an additional parameter and an added complexity that we decided to leave outside of the analysis at this time). Figure 5 shows the distribution of injection, pumping and observation wells: well #1 injects 16 m^3/d, well #2 injects 15 m^3/d, well #3 pumps 7.5 m^3/d, well #4 pumps 7.5 m^3/d, and well #5 pumps 14.5 m^3/d. The rest of the wells are used as observation wells, the state variables observed at these wells for the first 50 time steps (equivalent to 135.4 days) will be used in the assimilation step of the NS-EnKF algorithm described previously. In addition, wells #6, #7 and #8 are used as verification wells to evaluate the performance of the inversion beyond the assimilation period and up to 500 days. The initial head is set to 8 m throughout the whole domain.

For the modeling of solute transport, we consider advection, dispersion and linear sorption. The distribution coefficient k_d is $9.3{\cdot}10^{-4}$ m^3/kg. The longitudinal dispersivity is 1 m, and the transverse dispersivity is 0.01 m. The molecular diffusion coefficient D_m is set to zero. The solute is uniformly released along a line at $x = 8$ m (see Figure 3a). The source concentration is 50 mg/l. The initial solute concentration is set to zero throughout the whole domain.

For the modeling of heat transport, the density of the fluid ρ_w is 1000 kg/m^3, the density of the solid grains ρ_s is 2700 kg/m^3, the specific heat capacity of the fluid c_w is 4200 J/(kg$\cdot^o$K), the specific heat capacity of the solid c_s is 800 J/(kg$\cdot^o$K), the longitudinal dispersivity is 1 m, and the transversal dispersivity 0.01 m, the thermal conductivity of the fluid is 0.6 W/(m$\cdot^o$K), and the thermal conductivity of the solid is 2.2 W/(m$\cdot^o$K). Groundwater temperature along the solute release line (Figure 3a) is constant to 25 ^{o}C, and the temperature of the two injection wells #1 and #2 is also 25 ^{o}C. The initial temperature of the aquifer is 10 ^oC.

The total simulation time is 500 days, discretized into 100 time steps with increasing size following a geometric series with ratio 1.02. Observations of all three state variables are taken during 50 time steps (for a total of 135.4 days) and are used to update the augmented state as described above.

Seven scenarios are designed to analyze the trade-off between the different state variables for the purpose of characterizing the hydraulic conductivity and porosity fields. The combinations of conditioning information in each scenario are listed in Table 2.

4. Analysis

The aim of this section is to analyze how conditioning to different state variables influences the characterization of the hydraulic conductivity and porosity in a channelized aquifer. For this purpose, the NS-EnKF as described before is used. The conditions under which the analysis is performed are as follows:

- There are eight conditioning points for facies, porosity and hydraulic conductivity values, at the locations shown in Figure 2. These values are taken from the reference fields.

- The rest of the parameters, sinks and sources, and initial and boundary conditions are the same as for the reference case. Although this may seem unrealistic (neither the parameters will be homogeneous or perfectly known in a real case) it allows us to isolate the influence of porosity and hydraulic conductivity heterogeneity in the flow and transport and to measure how the use of observational data on the three state variables affects parameter characterization.

- The reference case has been modeled and the state variables have been retrieved at the end of each of the 50 time steps; these will be used as observational data for characterization purposes.

- An ensemble of 600 realizations of both hydraulic conductivity and porosity is generated conditioned to the 8 well values in Figure 2 following the same procedure as to generate the reference field, i.e., first a facies realizations is generated, then each facies is populated with parameter values.

- The multi-parameter multi-state-variable implementation of the NS-EnKF is run for 50 time steps. After each time step, the porosity and hydraulic conductivity fields are updated according to the Kalman filter equation (10).

Next, we analyze the seven scenarios in two aspects: the ability to capture the channel heterogeneity of both logconductivity and porosity reference fields, and the uncertainty associated to such a characterization.

Figure 6a, and Figure 6b show the $\ln K$ histogram and porosity histograms for the initial ensemble of 600 heterogeneous $\ln K$ and porosity realizations, respectively. Figure 7a-7g and Figure 8a-9g show the $\ln K$ histograms and porosity histograms for each scenario after the 50^{th} assimilation step. Comparing the updated histograms with the reference ones, we can see that the bimodality of the histograms of both $\ln K$ and porosity is retained in all scenarios. It is very important to note that the updated histograms have not drifted towards unimodal Gaussian distributions, as it would have happened if the standard implementation of the EnKF had been applied [*Zhou et al.*, 2011].

Figure 9 shows ensemble means and ensemble variances of the initial ensembles of realizations for both $\ln K$ and porosity. The heterogeneity associated with these initial ensembles is related to the different values at the eight conditioning points, but it is quite distant from the real channelized heterogeneity of the reference.

Figure 10 and Figure 11 show the ensemble means of the updated $\ln K$ realizations after the 10^{th} and the 50^{th} assimilation time step, respectively for all seven scenarios. Their corresponding ensemble variances are shown in Figure 12 and Figure 13. Similarly, Figure

14 and Figure 15 show the ensemble means of the updated porosity realizations after the 10^{th} and the 50^{th} assimilation time step, respectively. And, Figure 16 and Figure 17 show the corresponding ensemble variances.

From a visual analysis of the above mentioned figures it is clear that, in all scenarios, assimilating the transient behavior of one or several state variables helps in delineating the underlying heterogeneity; and that this delineation improves as time passes by and is better when all state variables are assimilated. It is also clear that not all state variables have the same information content regarding the characterization of the two parameters of interest. Comparing the different scenarios we could reach the following conclusions:

- It is best to use all the state variables. Scenario S4 uses the data from the three state variables to update the parameter fields, and reaches the best approximation after 50 time steps, and also the smallest local uncertainties.

- The worst results are obtained when only solute concentration is assimilated. The results are still good, but neither the channels are so well identified nor the uncertainty reduced as much. The reason for this result lies in the slower movement of the solute plume as compared to the movement of the temperature plume, which diffuses strongly.

- The state variables dependent on fluid advection introduce a clear improvement in the characterization at the latter time steps; parameter variances, especially that of hydraulic conductivity is quite high at the $10th$ time step for those scenarios that do not assimilate piezometric heads, but this variance reduces drastically at the $50th$ time step and becomes similar to the variances of the other scenarios (except for scenario S5, which only assimilates concentration data). This behavior is because many of the observation wells are "inactive" during the initial time steps and do not sample neither the solute nor the variations in temperature.

- For this particular case, assimilating temperature seems to be more beneficial than assimilating concentrations, because temperature migrates faster than the solute and therefore, at the same time step, it carries more spatial information than by the concentrations. But this result is specific of this example, for a different combination of parameters describing the mass and heat transport, the reverse could be true.

- In general, it is best to assimilate two state variables than just one, except as mentioned before for earlier time steps in which the assimilation of piezometric heads can be more beneficial than assimilating variables dependent on advection.

In order to perform a more quantitative comparison between the different scenarios, and taking advantage that we have access to the underlying truth (the reference fields) we can compute the square root of the mean square error, $RMSE$, and the square root of the ensemble variance, ES, for each of the parameters of interest as:

$$RMSE_i = \sqrt{\frac{1}{N}\sum_{j=1}^{N}(P_i(j)^{ref} - \langle P_i(j)\rangle)^2}, \quad i = 1, \ldots, l. \tag{12}$$

$$ES_i = \sqrt{\frac{1}{N}\sum_{j=1}^{N}\sigma^2_{P_i(j)}}, \quad i = 1, \ldots, l. \tag{13}$$

where N is the number of model elements; $P_i(j)^{ref}$ is the i^{th} hydraulic parameter at node j in the reference field; $\langle P_i(j)\rangle$ is the ensemble mean, and $\sigma^2_{P_i(j)}$ is the ensemble variance.

The $RMSE$ and ES values should be comparable in magnitude and are a quantitative measure of the accuracy and precision, respectively, with which the updated fields reproduce the reference fields. Optimally, both values should tend to zero as the characterization improves.

Figure 18 shows the evolution in time of the $RMSE$ and ES for both ln$K$ and porosity and for all scenarios. As anticipated in the visual analysis, scenario S4 displays the smallest $RMSE$ at time step 50, and also the largest reduction of ensemble variance with time, together with scenario S3 . When only piezometric heads are used (scenario S1), there is a time, around the 15^{th} time step, after which only a marginal improvement is obtained with the assimilation of additional data; whereas, when other state variables are used jointly with the piezometric heads, we can see that the improvement for both $RMSE$ and ES continues past time step 15 (more notably for ln$K$). It is also interesting to note that, about time step 25, the $RMSE$ and ES curves for the scenarios S6 and S7 (assimilating temperature or temperature and solute concentration) cross the curve for scenario S1, marking a trade-off point: before that time, assimilating only piezometric head is more informative than assimilating only temperature (or temperature and solute concentration jointly), but, after that time, the roles are exchanged, and it is better to assimilate temperature than piezometric heads.

Figure 19 shows the evolution in time of the piezometric heads (in the top row), the solute concentrations (in the middle row) and the temperatures (in the bottom row) at verification wells #6, #7 and #8 for the initial ensemble of ln$K$ and porosity fields. Each solid curve corresponds to one of the ensemble members, and the green curve is the mean of the 600 solid curves. For comparison, the red curve shows the evolution in the reference field. The vertical dashed line shows the period at which assimilation stops (time step number 50, equivalent to 135.4 days). Since none of these ensemble members account for any state variable, the spread of these curves is extreme.

Figures 20, 21 and 22 are similar to Figure 19 with the evolution of the state variables computed on the updated parameter fields after 50 assimilation steps. More precisely, Figure 20 shows piezometric heads, Figure 21 shows solute concentrations, and Figure 22 shows temperature, all three Figures for all scenarios S1-S7. From the analysis of these figures we can conclude that: (i) the spread of all state variables is greatly reduced after updating the parameter fields through the assimilation of the observations; (ii) piezometric heads are almost perfectly reproduced in the updated parameter fields, when the piezometric heads are being assimilated, with the best results for scenario S4; (iii) there is also an improvement in the reproduction of the heads when they are not assimilated, especially for scenarios S6 and S7, the improvement for scenario S5 is lesser, indicating that solute concentrations alone do not carry much information about the piezometric head evolution during the first 50 time steps; (iv) solute concentrations, when assimilated, are greatly improved, specially for scenarios S4 and S7, but not as much as the piezometric heads; (v) when solute concentrations are not assimilated, the improvement is clear if temperatures are assimilated, since it is another variable subject to advection-dispersion; (vi) temperatures are also greatly improved, when included in the assimilation, but again not as much as the piezometric heads; (vii) when temperatures are not assimilated, the improvement is more noticeable if concentrations are observed, for the same reason mentioned before for the temperatures; (viii) for solute concentration and temperature, the well configuration has a clear impact on the ability of reproducing the observed state variables, since well

#6 is connected to well #1 and to the upper zone of the solute release zone through the top channel, and transport is more affected by such a channeling than piezometric heads.

5. Summary and conclusion

In this paper, we have presented an extension of the normal-score ensemble Kalman filter to work with multiple state variables for the characterization of several parameters whose spatial variability follows non-Gaussian distributions. Specifically, the NS-EnKF has been applied for the characterization of hydraulic conductivity and porosity fields by the assimilation of piezometric heads, solute concentrations and temperature data. As expected, the larger the number of state variables used and the longer the assimilation period, the better the characterization of both fields. By analyzing different combinations of the different state variables, we realize that the information content on the observed variables varies as a function of time; in particular, in this specific example, there is a point in time up to which it is best to assimilate piezometric heads, but after which the assimilation of temperature data produces better results. The main conclusion from this demonstration is that there are tools capable to account for different sources of data when characterizing complex aquifer heterogeneities, and that they should be considered in real applications in order to effectively produce realistic models of heterogeneity with associated uncertainties.

Acknowledgments. Financial support to carry out this work was provided by the Spanish Ministry of Economy and Competitiveness through project CGL2014-59841-P. All data used in this analysis are available from the authors.

References

Alcolea, A., J. Carrera, and A. Medina (2006), Pilot points method incorporating prior information for solving the groundwater flow inverse problem, *Advances in Water Resources*, *29*(11), 1678–1689.

Anderson, M. P. (2005), Heat as a ground water tracer, *Groundwater*, *43*(6), 951–968.

Bear, J. (1972), *Dynamics of fluids in porous media.*, American Elsevier Pub. Co., New York, 764pp.

Bravo, H. R., F. Jiang, and R. J. Hunt (2002), Using groundwater temperature data to constrain parameter estimation in a groundwater flow model of a wetland system, *Water Resources Research*, *38*(8), 28–1.

Capilla, J. E., and C. Llopis-Albert (2009), Gradual conditioning of non-gaussian transmissivity fields to flow and mass transport data: 1. theory, *Journal of hydrology*, *371*(1), 66–74.

Chang, H., D. Zhang, and Z. Lu (2010), History matching of facies distribution with the enkf and level set parameterization, *Journal of Computational Physics*, *229*(20), 8011–8030.

Chen, Y., and D. Oliver (2010), Parameterization techniques to improve mass conservation and data assimilation for ensemble kalman filter, in *SPE Western Regional Meeting*.

Chen, Y., D. Oliver, and D. Zhang (2009), Data assimilation for nonlinear problems by ensemble kalman filter with reparameterization, *Journal of Petroleum Science and Engineering*, *66*(1), 1–14.

Doherty, J., L. Brebber, and P. Whyte (1994), Pest: Model-independent parameter estimation, *Watermark Computing, Corinda, Australia*, *122*.

Doussan, C., A. Toma, B. Paris, G. Poitevin, E. Ledoux, and M. Detay (1994), Coupled use of thermal and hydraulic head data to characterize river-groundwater exchanges, *Journal of Hydrology*, *153*(1), 215–229.

Dovera, L., and E. Della Rossa (2011), Multimodal ensemble kalman filtering using gaussian mixture models, *Computational Geosciences*, *15*(2), 307–323.

Evensen, G. (2003), The ensemble kalman filter: Theoretical formulation and practical implementation, *Ocean Dynamics*, *53*(4), 343–367.

Franssen, H.-J. H., J. Gómez-Hernández, and A. Sahuquillo (2003), Coupled inverse modelling of groundwater flow and mass transport and the worth of concentration data, *Journal of Hydrology*, *281*(4), 281–295.

Fu, J., and J. J. Gómez-Hernández (2009), Uncertainty assessment and data worth in groundwater flow and mass transport modeling using a blocking markov chain monte carlo method, *Journal of Hydrology*, *364*(3), 328–341.

Gómez-Hernández, J., and X.-H. Wen (1994), Probabilistic assessment of travel times in groundwater modeling, *Stochastic Hydrology and Hydraulics*, *8*(1), 19–55.

Gómez-Hernández, J. J., and A. G. Journel (1993), Joint sequential simulation of multi-Gaussian fields, *Geostatistics Troia*, *92*(1), 85–94.

Gómez-Hernández, J. J., H. J. W. M. Hendricks Franssen, and A. Sahuquillo (2003), Stochastic conditional inverse modeling of subsurface mass transport: A brief review and the self-calibrating method, *Stochastic Environmental Research and Risk Assessment*, *17*(5), 319–328.

Gómez-Hernánez, J., A. Sahuquillo, and J. Capilla (1997), Stochastic simulation of transmissivity fields conditional to both transmissivity and piezometric data–1. theory, *Jour-*

nal of Hydrology(Amsterdam), *203*(1), 167–174.

Gordon, N., D. Salmond, and A. Smith (1993), Novel approach to nonlinear/non-gaussian bayesian state estimation, in *Radar and Signal Processing, IEE Proceedings F*, vol. 140, pp. 107–113, IET.

Gu, Y., and D. Oliver (2006), The ensemble kalman filter for continuous updating of reservoir simulation models, *TRANSACTIONS-AMERICAN SOCIETY OF MECHANICAL ENGINEERS JOURNAL OF ENERGY RESOURCES TECHNOLOGY*, *128*(1), 79.

Gu, Y., and D. Oliver (2007), An iterative ensemble kalman filter for multiphase fluid flow data assimilation, *SPE Journal*, *12*(4), 438–446.

Healy, R. W., and A. D. Ronan (1996), *Documentation of computer program VS2DH for simulation of energy transport in variably saturated porous media: Modification of the US Geological Survey's computer program VS2DT*, US Geological Survey.

Hu, L. (2000), Gradual deformation and iterative calibration of gaussian-related stochastic models, *Mathematical Geology*, *32*(1), 87–108.

Kalman, R., et al. (1960), A new approach to linear filtering and prediction problems, *Journal of basic Engineering*, *82*(1), 35–45.

Kurtz, W., H.-J. Hendricks Franssen, H.-P. Kaiser, and H. Vereecken (2014), Joint assimilation of piezometric heads and groundwater temperatures for improved modeling of river-aquifer interactions, *Water Resources Research*, *50*(2), 1665–1688.

Li, L., H. Zhou, J. J. Gómez-Hernández, and H.-J. H. Franssen (2012a), Jointly mapping hydraulic conductivity and porosity by assimilating concentration data via ensemble kalman filter, *Journal of Hydrology*, *428*, 152–169.

Li, L., H. Zhou, H. Hendricks Franssen, and J. Gómez-Hernández (2012b), Groundwater flow inverse modeling in non-multigaussian media: performance assessment of the normal-score ensemble kalman filter, *Hydrology and Earth System Sciences*, *16*(2), 573.

Li, L., H. Zhou, H.-J. H. Franssen, and J. J. Gómez-Hernández (2012c), Groundwater flow inverse modeling in non-multigaussian media: performance assessment of the normal-score ensemble kalman filter, *Hydrology and Earth System Sciences and Discussions*, *16*(2), 573–590.

Liu, N., and D. Oliver (2005), Critical evaluation of the ensemble kalman filter on history matching of geologic facies, in *SPE Reservoir Simulation Symposium*.

Losa, S., G. Kivman, J. Schröter, and M. Wenzel (2003), Sequential weak constraint parameter estimation in an ecosystem model, *Journal of Marine Systems*, *43*(1), 31–49.

Ma, R., and C. Zheng (2010), Effects of density and viscosity in modeling heat as a groundwater tracer, *Groundwater*, *48*(3), 380–389.

Ma, R., C. Zheng, J. M. Zachara, and M. Tonkin (2012), Utility of bromide and heat tracers for aquifer characterization affected by highly transient flow conditions, *Water Resources Research*, *48*(8).

McDonald, M., and A. Harbaugh (1988), A modular three-dimensional finite-difference ground-water flow model.

Oliver, D., L. Cunha, and A. Reynolds (1997), Markov chain monte carlo methods for conditioning a permeability field to pressure data, *Mathematical Geology*, *29*(1), 61–91.

RamaRao, B., A. LaVenue, G. De Marsily, and M. Marietta (1995), Pilot point methodology for automated calibration of an ensemble of conditionally simulated transmissivity fields: 1. theory and computational experiments, *Water Resources Research*, *31*(3), 475–493.

Reich, S. (2011), A gaussian-mixture ensemble transform filter, *Quarterly Journal of the Royal Meteorological Society*, *138*(662), 222–233.

Simon, E., and L. Bertino (2009), Application of the gaussian anamorphosis to assimilation in a 3-d coupled physical-ecosystem model of the north atlantic with the enkf: a twin experiment, *Ocean Science*, *5*(4), 495–510.

Strebelle, S. (2002), Conditional simulation of complex geological structures using multiple-point statistics, *Mathematical Geology*, *34*(1), 1–21.

Sun, A., A. Morris, and S. Mohanty (2009), Sequential updating of multimodal hydrogeologic parameter fields using localization and clustering techniques, *Water Resources Research*, *45*(7), W07,424.

Van Leeuwen, P. (2009), Particle filtering in geophysical systems, *Monthly Weather Review*, *137*(12), 4089–4114.

Wang, Y., G. Li, and A. Reynolds (2010), Estimation of depths of fluid contacts by history matching using iterative ensemble-kalman smoothers, *SPE Journal*, *15*(2), 509–525.

Wen, X., and W. Chen (2006), Real-time reservoir model updating using ensemble kalman filter with confirming option, *SPE Journal*, *11*(4), 431–442.

Wen, X., C. Deutsch, and A. Cullick (2002), Construction of geostatistical aquifer models integrating dynamic flow and tracer data using inverse technique, *Journal of Hydrology*, *255*(1), 151–168.

Wen, X. H., J. E. Capilla, C. V. Deutsch, J. J. Gómez-Hernández, and A. S. Cullick (1999), A program to create permeability fields that honor single-phase flow rate and pressure data, *Computers & Geosciences*, *25*(3), 217–230.

Xu, T., and J. J. Gómez-Hernández (2015a), Inverse sequential simulation: A new approach for the characterization of hydraulic conductivities demonstrated on a non-gaussian field, *Water Resources Research*, *51*(4), 2227–2242.

Xu, T., and J. J. Gómez-Hernández (2015b), Inverse sequential simulation: Performance and implementation details, *Advances in Water Resources*, *86*, 311–326.

Xu, T., J. J. Gómez-Hernández, H. Zhou, and L. Li (2013), The power of transient piezometric head data in inverse modeling: an application of the localized normal-score enkf with covariance inflation in a heterogenous bimodal hydraulic conductivity field, *Advances in Water Resources*, *54*, 100–118.

Zheng, C. (2010), *Tech. rep.*, Technical Report to the US Army Engineer Research and Development Center.

Zhou, H., J. Gómez-Hernández, H. Hendricks Franssen, and L. Li (2011), An approach to handling non-gaussianity of parameters and state variables in ensemble kalman filtering, *Advances in Water Resources*, *34*(7), 844–864.

Zhou, H., L. Li, H. Hendricks Franssen, and J. Gómez-Hernández (2012), Pattern recognition in a bimodal aquifer using the normal-score ensemble kalman filter, *Mathematical Geosciences*, pp. 1–17.

Zhou, H., J. J. Gómez-Hernández, and L. Li (2014), Inverse methods in hydrogeology: evolution and recent trends, *Advances in Water Resources*, *63*, 22–37.

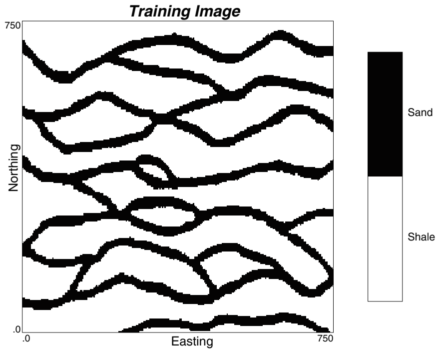

Figure 1. Training image

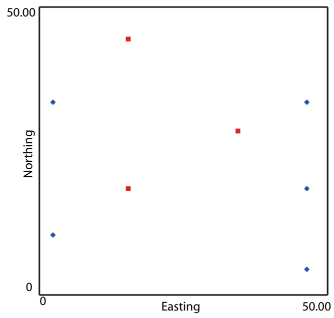

Figure 2. Conditional data locations. The red nodes are in the low permeability/high porosity material; the green nodes are in the high permeability/medium porosity material.

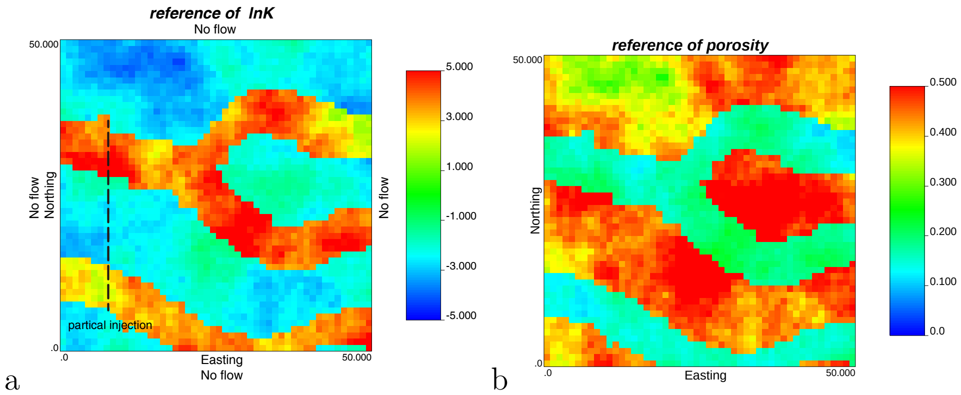

Figure 3. Reference fields of $\ln K$ and porosity. The dashed line is the source line for solute release into the aquifer.

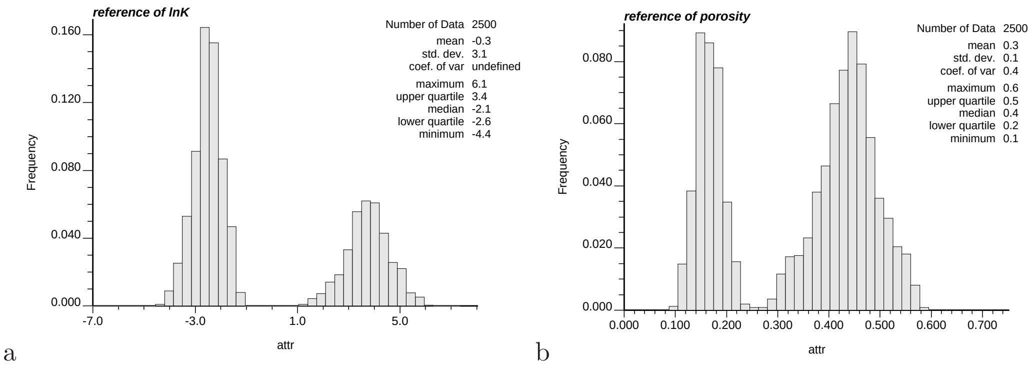

Figure 4. Histogram of ln$K$ and porosity from the reference fields

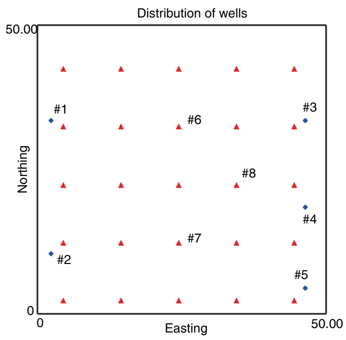

Figure 5. Well locations. Red triangles denote observation wells; blue squares denote injection (#1, #2) and pumping wells (#3, #4 and #5). The observation wells labeled #6, #7, #8 are used as verification wells.

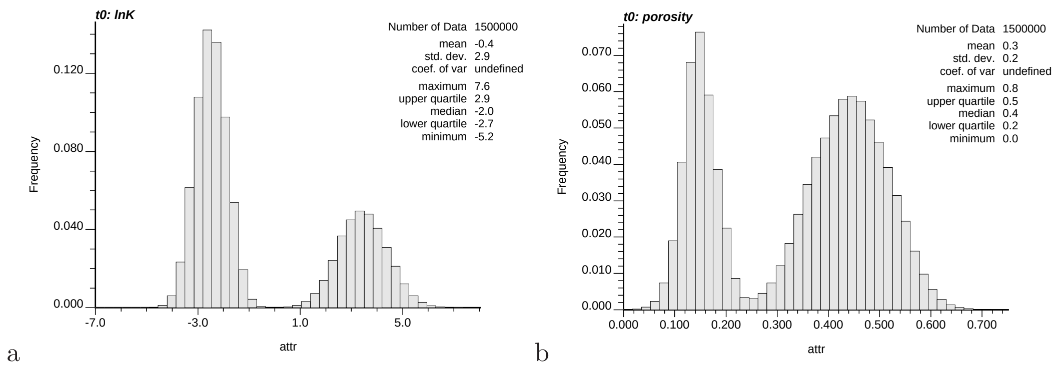

Figure 6. Histogram of the initial ensemble of ln$K$ and porosity realizations

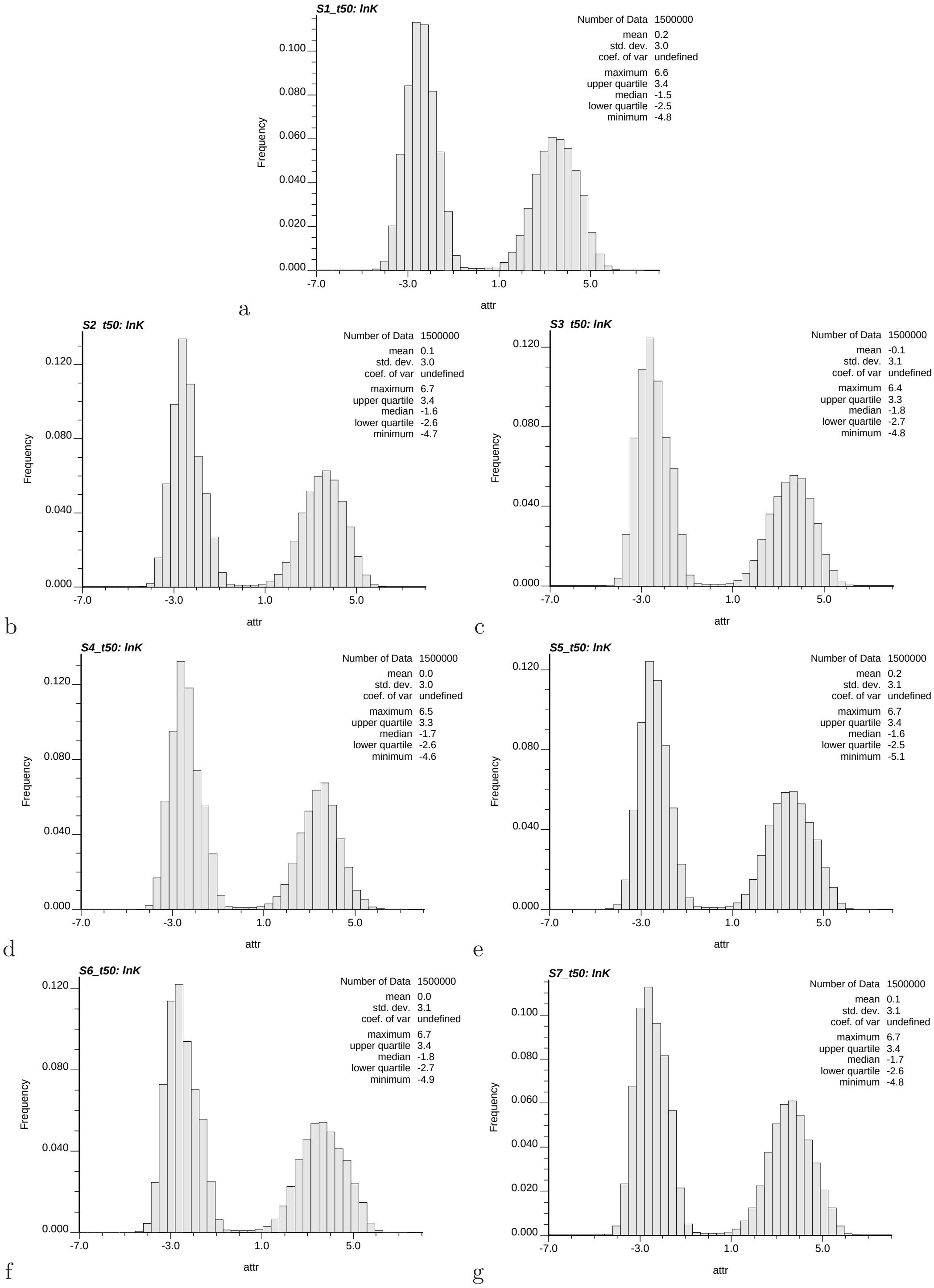

Figure 7. Scenarios S1-S7. Histogram of ln$K$ for the updated ensemble of realizations after the 50^{th} assimilation step.

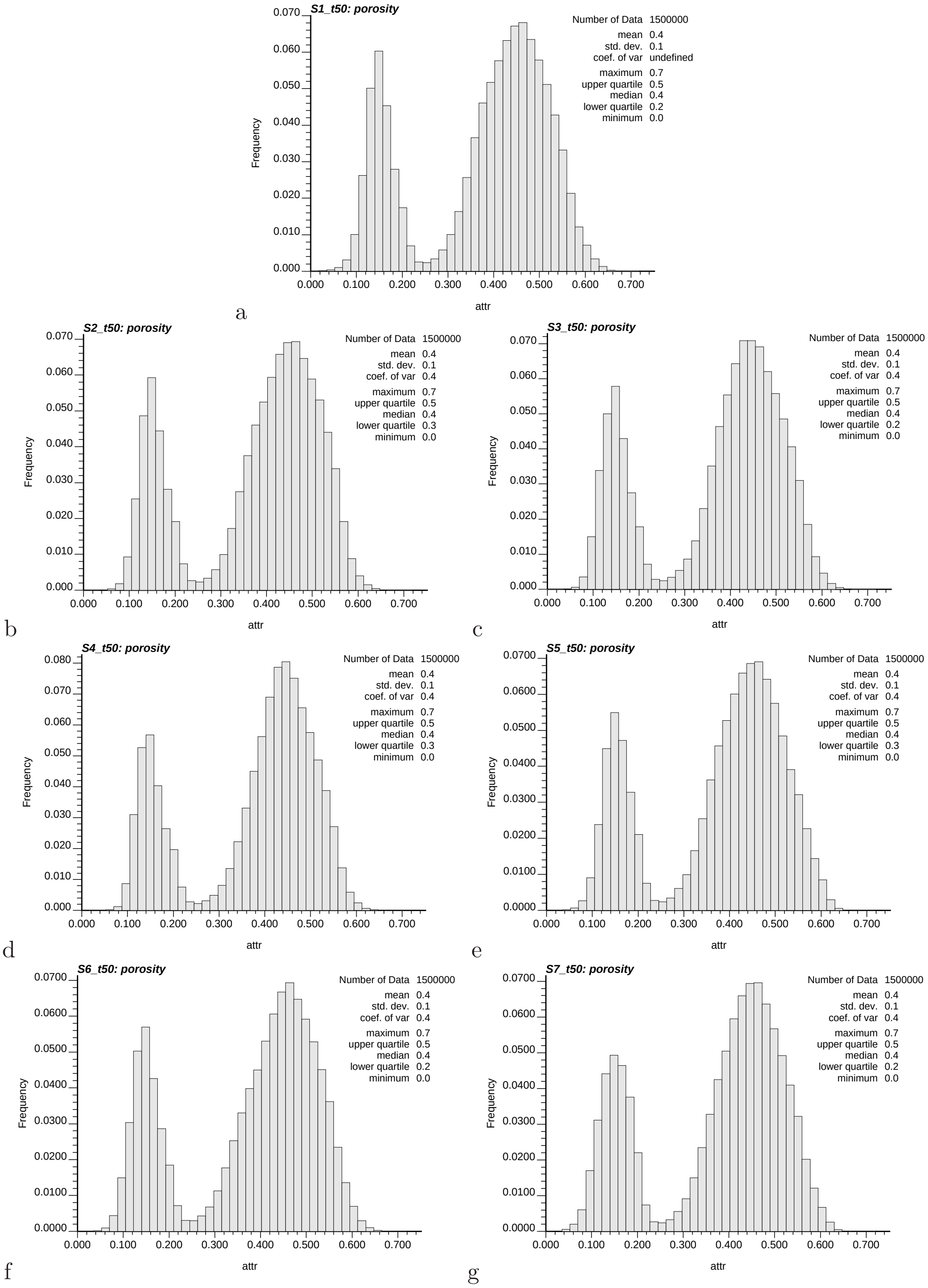

Figure 8. Scenarios S1-S7. Histogram of porosity for the updated ensemble of realizations after the 50^{th} assimilation step.

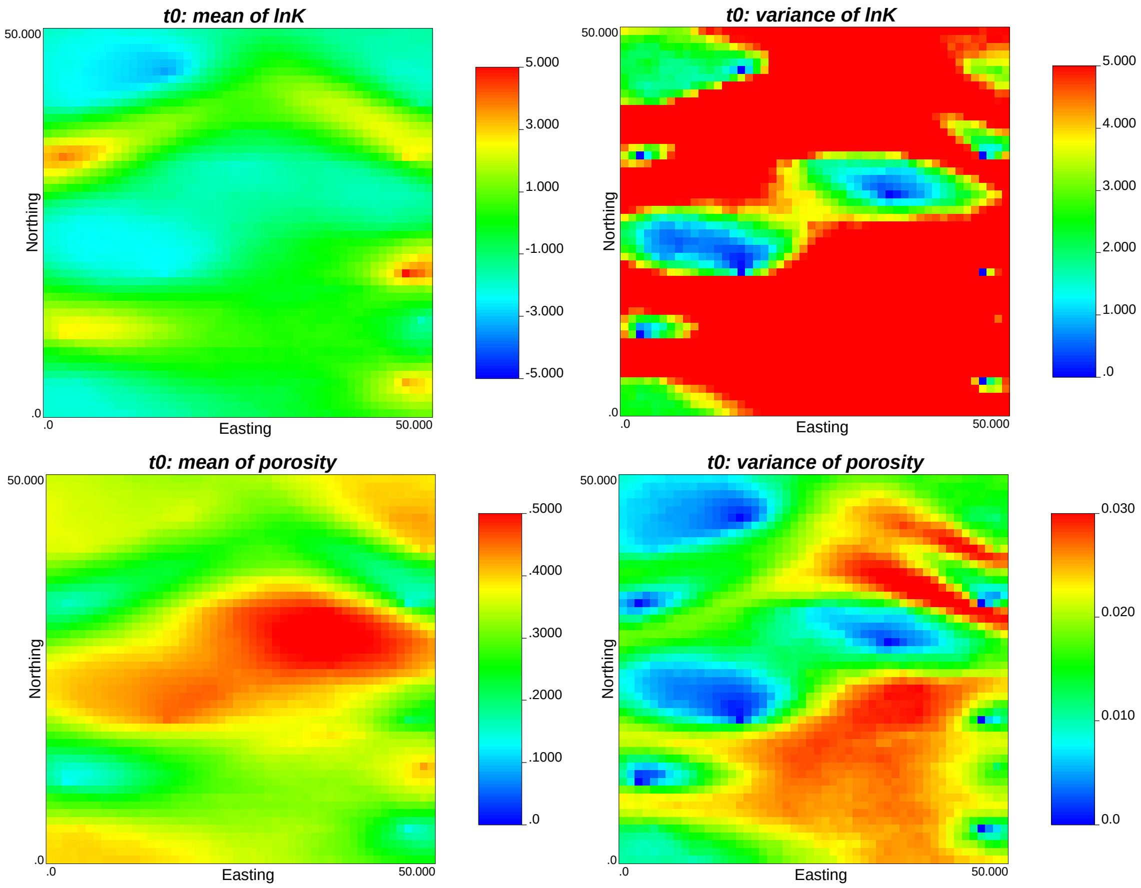

Figure 9. Ensemble mean and ensemble variance of the initial ensemble of realizations for $\ln K$ (top) and porosity (bottom).

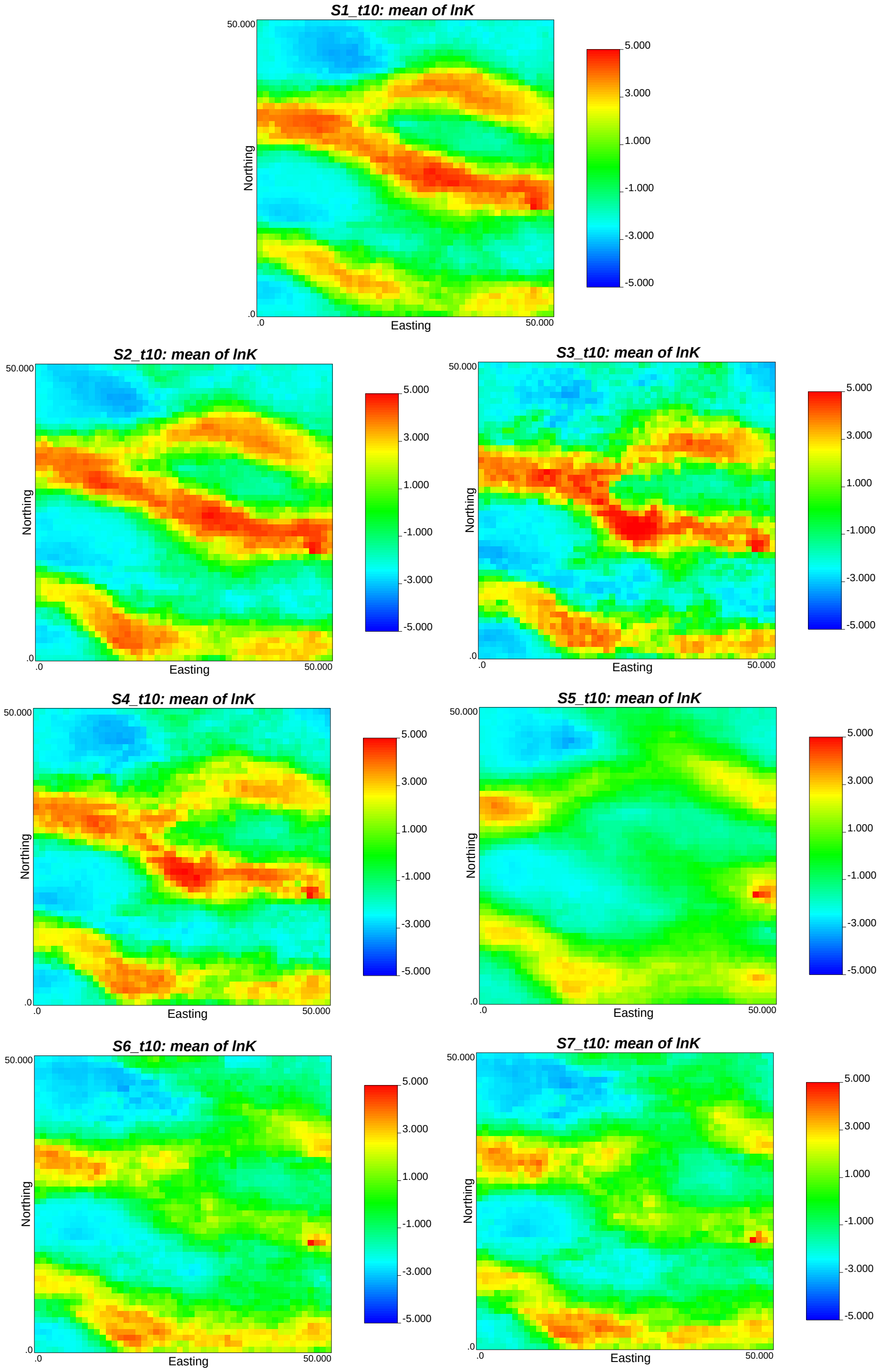

Figure 10. Scenarios S1-S7. Ensemble mean of ln$K$ for the updated ensemble of realizations after the 10^{th} assimilation step.

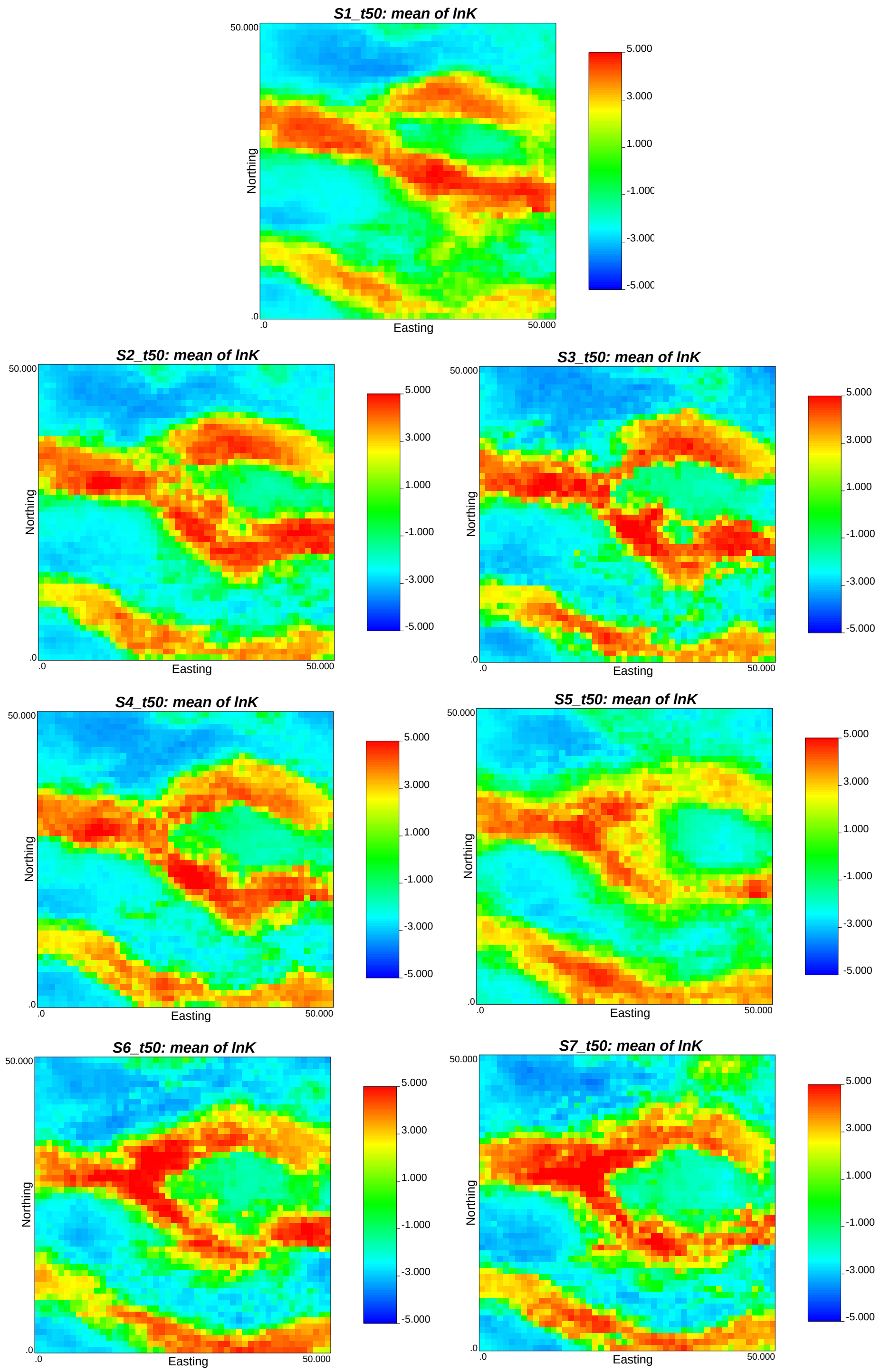

Figure 11. Scenarios S1-S7. Ensemble mean of $\ln K$ for the updated ensemble of realizations after the 50^{th} assimilation step.

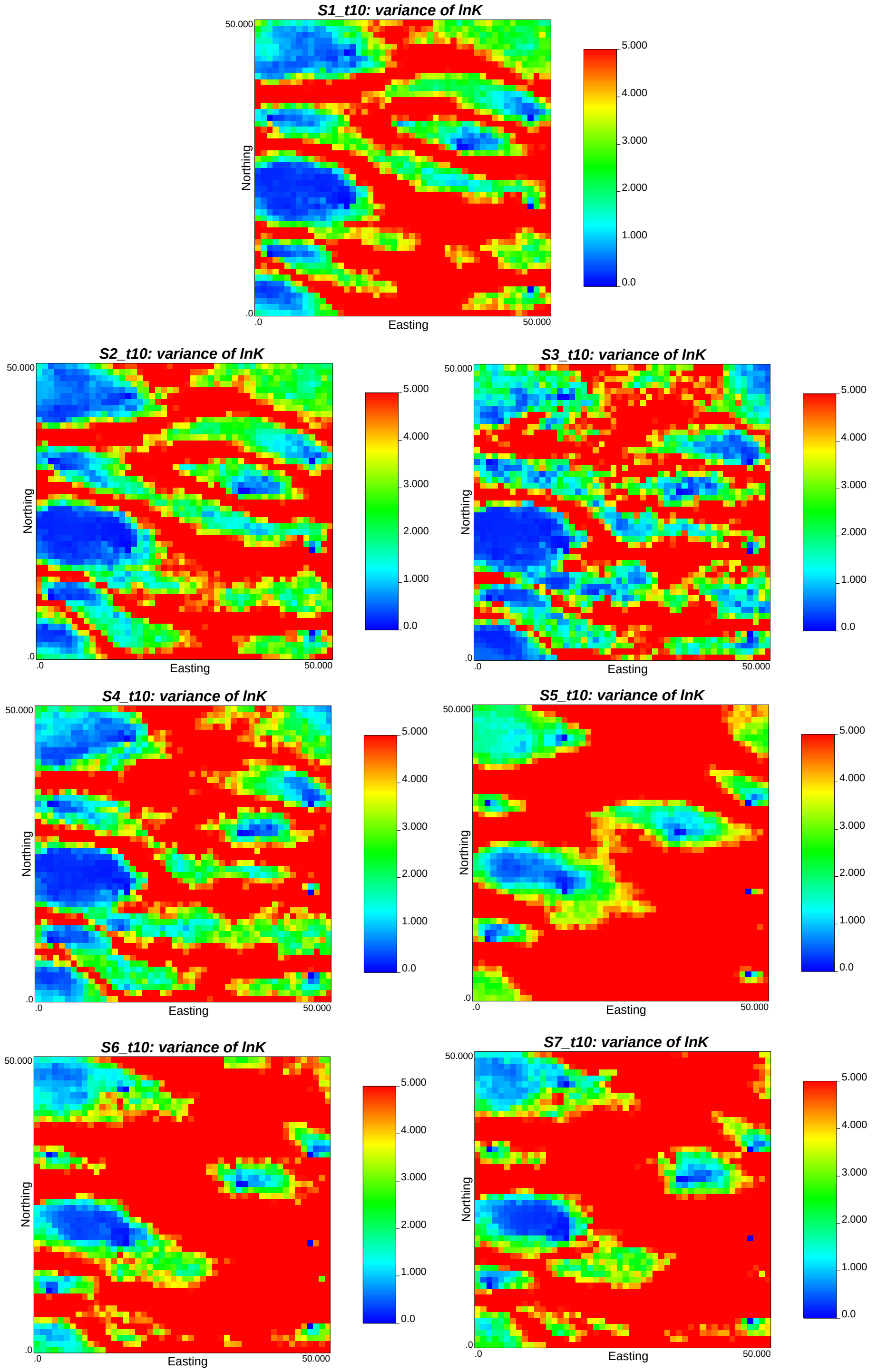

Figure 12. Scenarios S1-S7. Ensemble variance of $\ln K$ for the updated ensemble of realizations after the 10^{th} assimilation step.

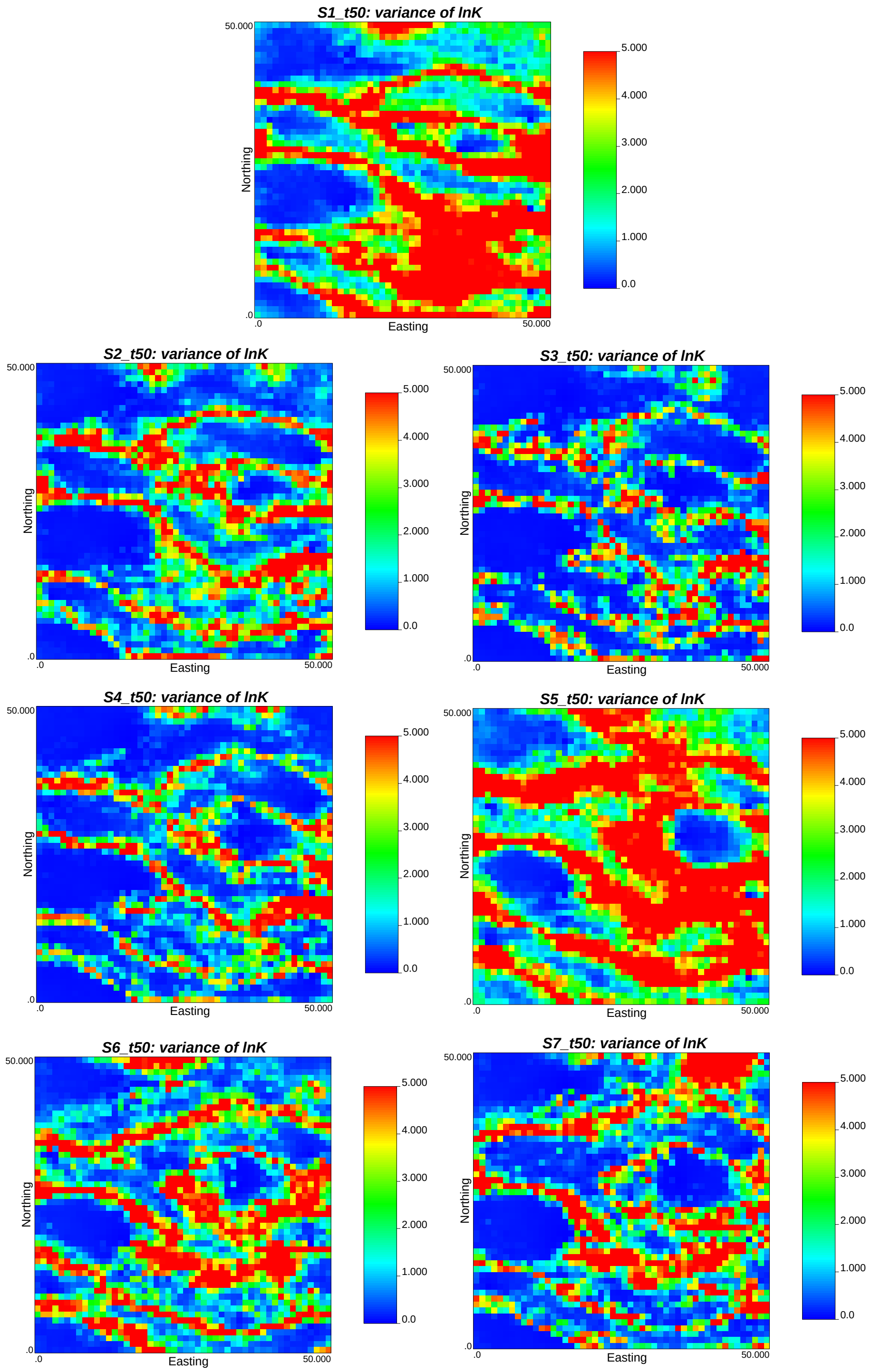

Figure 13. Scenarios S1-S7. Ensemble variance of $\ln K$ for the updated ensemble of realizations after the 50^{th} assimilation step.

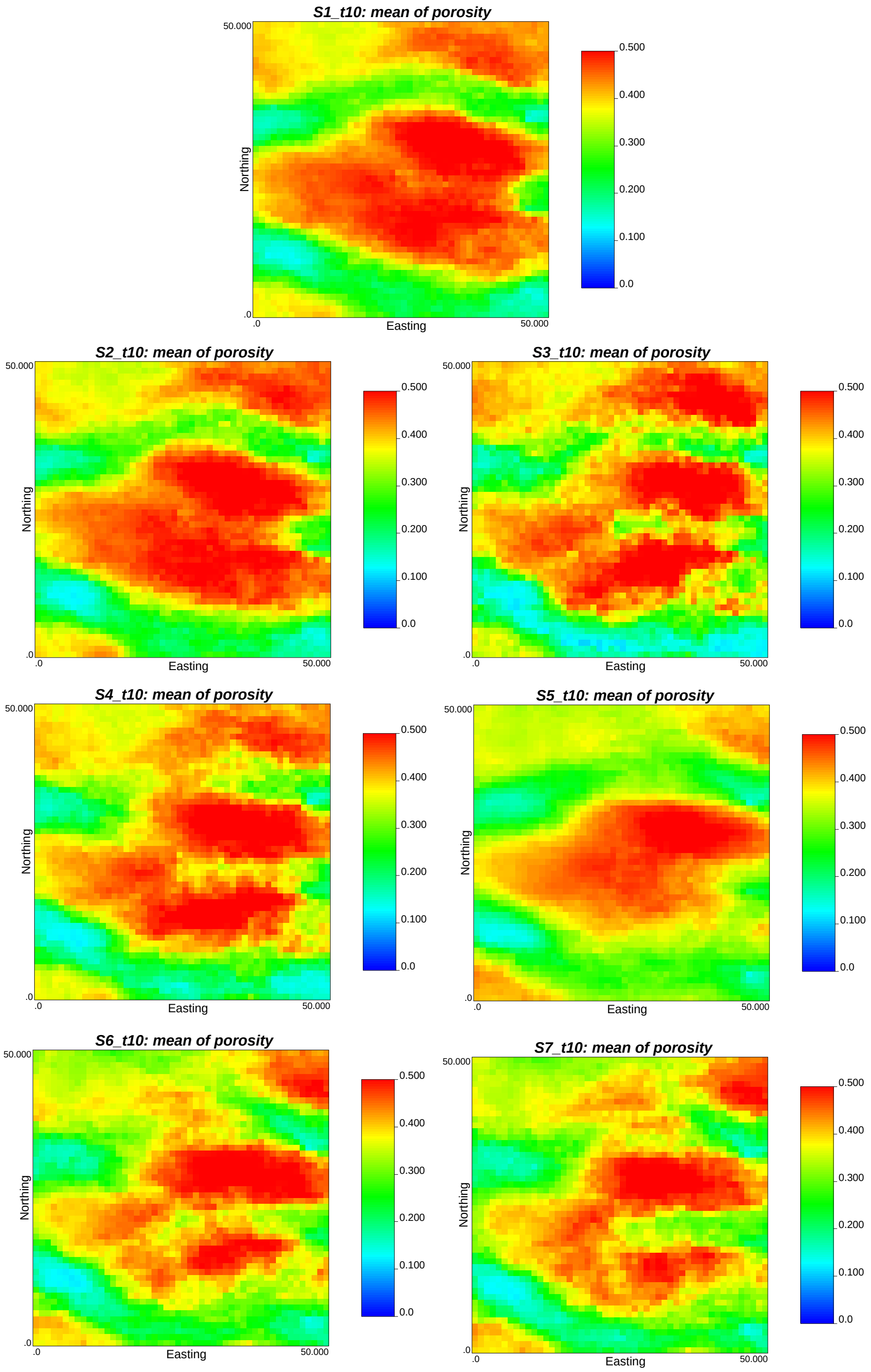

Figure 14. Scenarios S1-S7. Ensemble mean of porosity for the updated ensemble of realizations after the 10^{th} assimilation step.

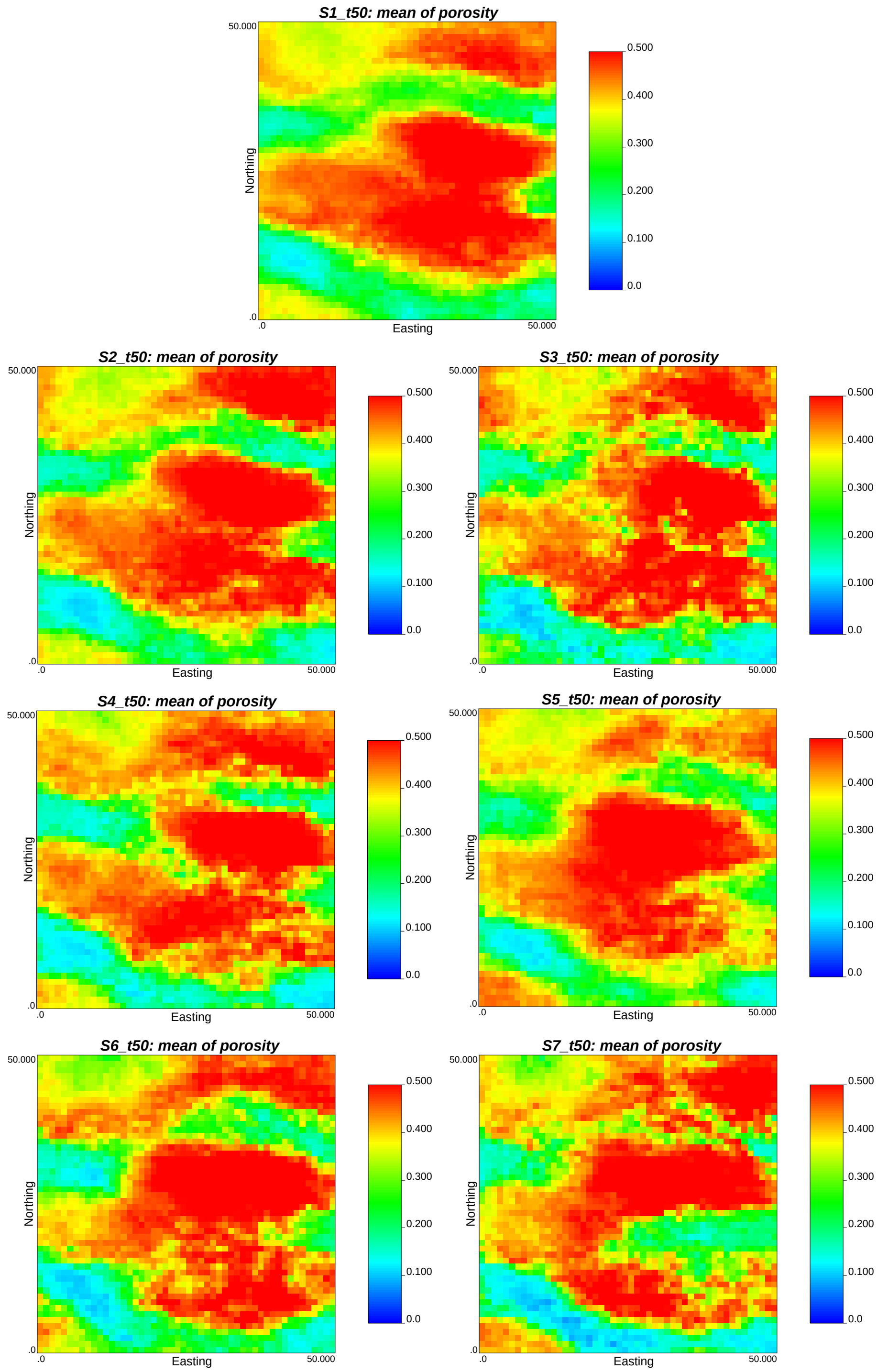

Figure 15. Scenarios S1-S7. Ensemble mean of porosity for the updated ensemble of realizations after the 50^{th} assimilation step.

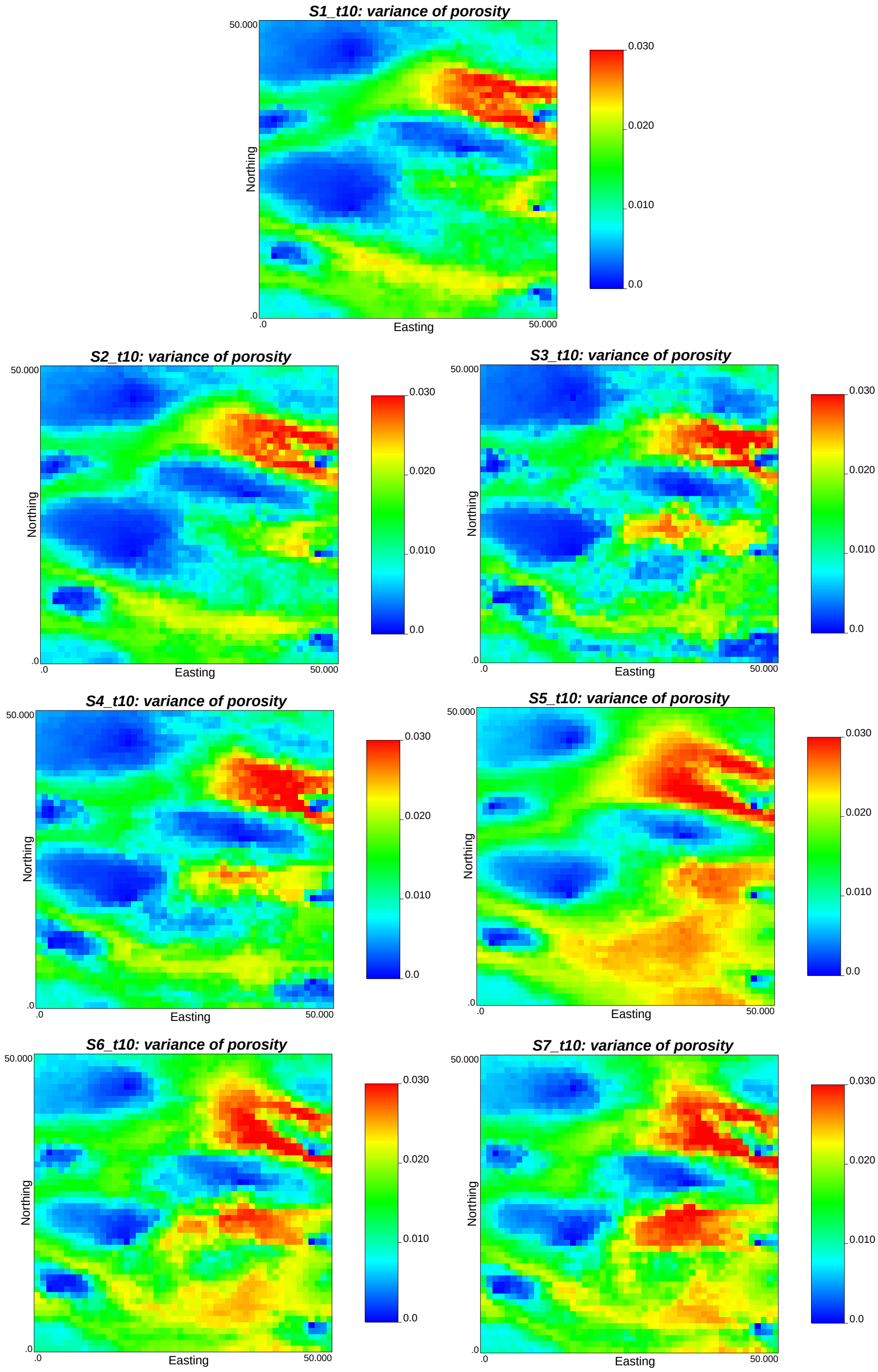

Figure 16. Scenarios S1-S7. Ensemble variance of porosity for the updated ensemble of realizations after the 10^{th} assimilation step.

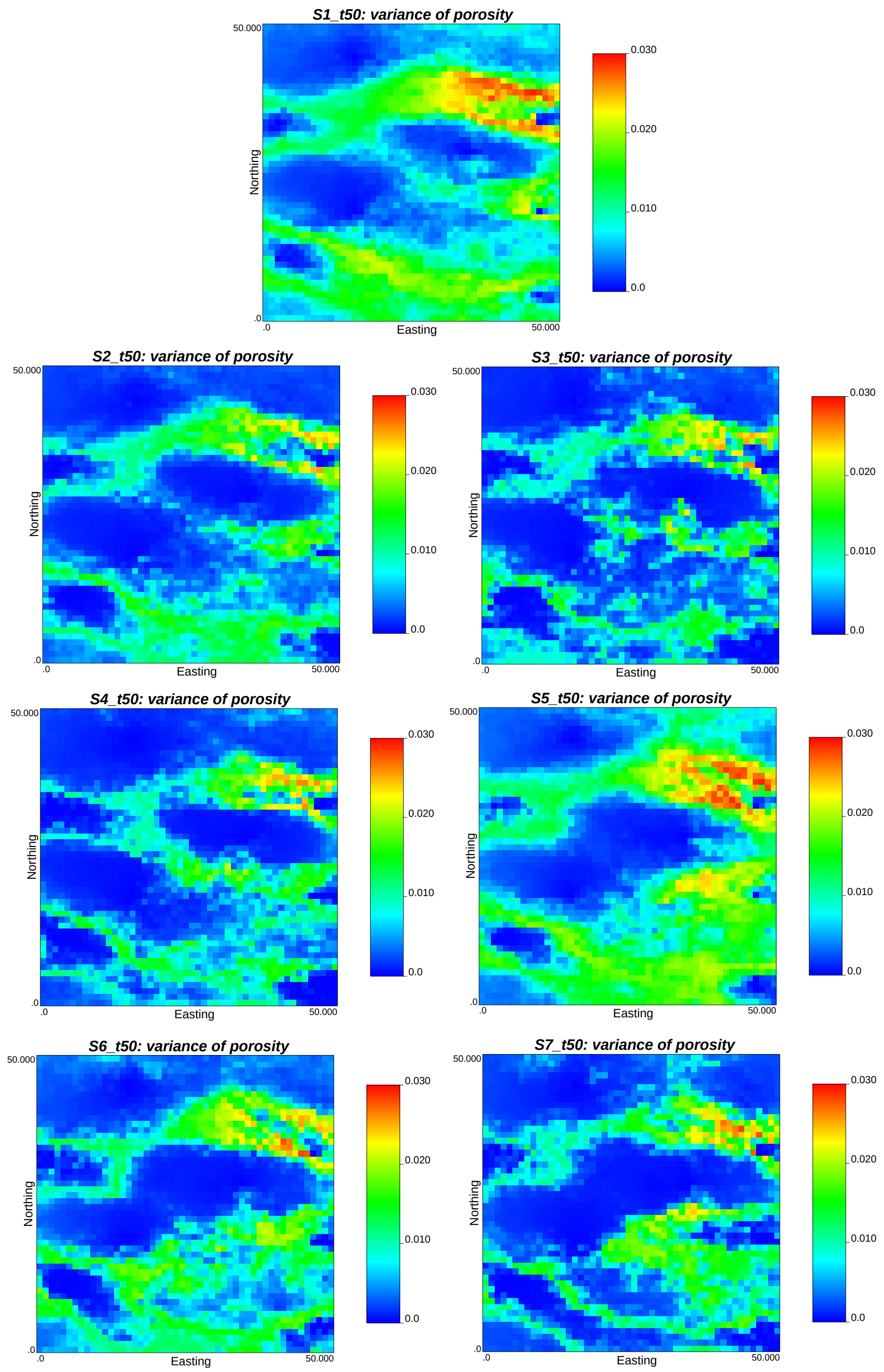

Figure 17. Scenarios S1-S7. Ensemble variance of porosity for the updated ensemble of realizations after the 50^{th} assimilation step.

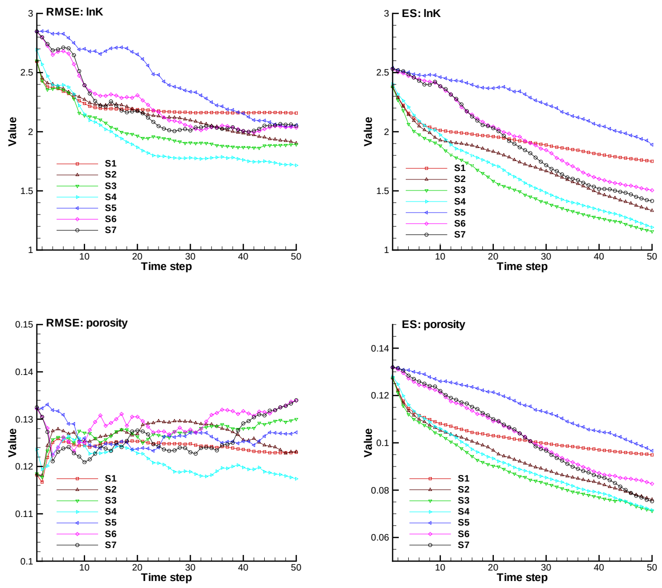

Figure 18. RMSE and ES as a function of time for all scenarios.

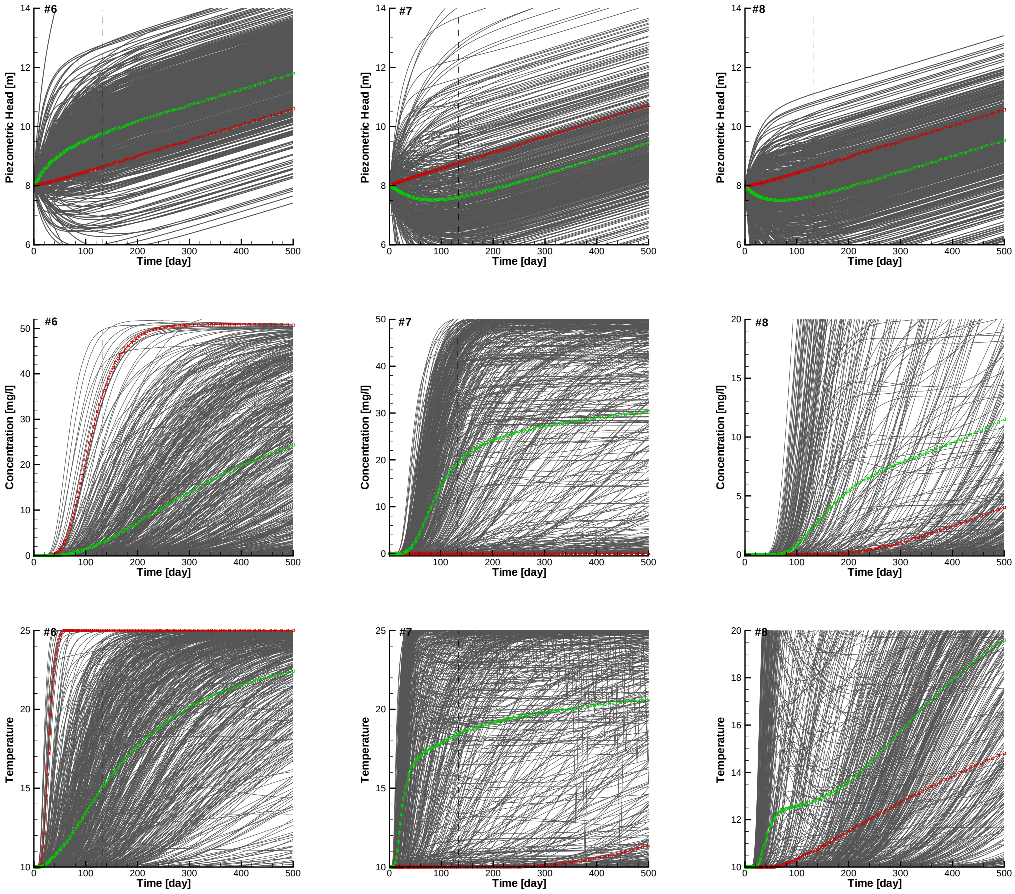

Figure 19. Evolution in time of piezometric head (top), solute concentration (middle) and temperature (bottom) at the three verification wells for the initial ensemble of porosity and log-conductivity realizations. Each black solid line corresponds to a member of the ensemble. The green line is the average of all ensemble curves. The red line corresponds to the evolution of the state variable in the reference. The vertical dashed lines marks the end of the state data assimilation period.

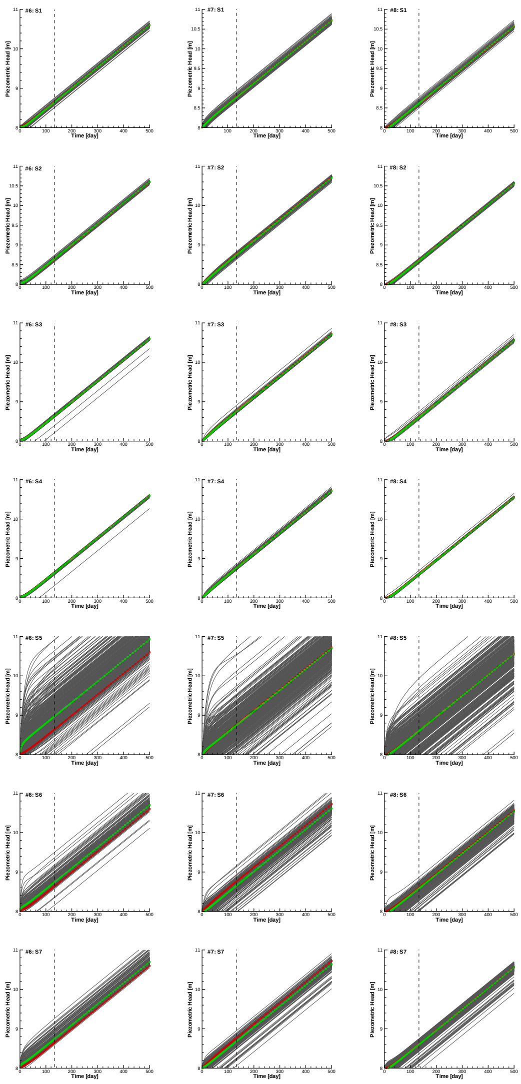

Figure 20. Evolution in time of the piezometric head at the three verification wells with the $\ln K$ and porosity fields obtained after the 50th assimilation time step for scenarios S1-S7. Each black solid line corresponds to a member of the ensemble. The green line is the average of all ensemble curves. The red line corresponds to the evolution of the state variable in the reference. The vertical dashed lines marks the end of the state data assimilation period.

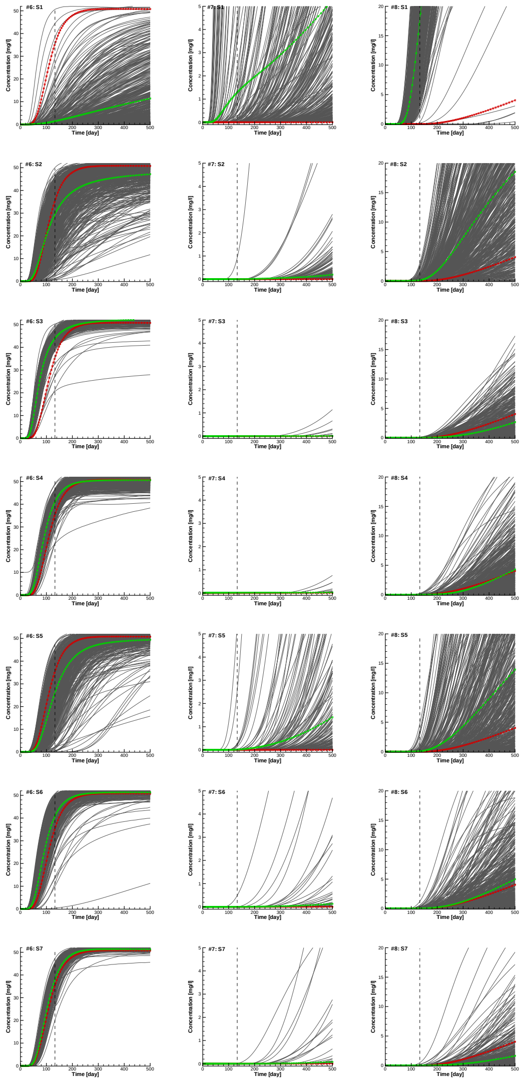

Figure 21. Same caption as previous figure but now for solute concentration.

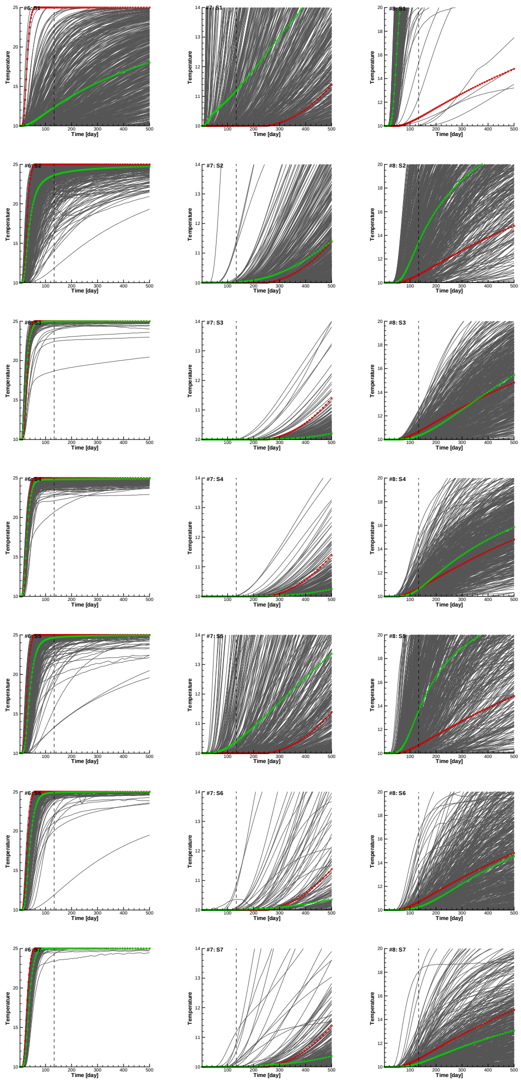

Figure 22. Same caption as previous figure but now for fluid temperature.

Table 1. Parameters of the random functions describing the heterogeneity of ln$K$ and porosity for the two materials. λ_x and λ_y are the correlation ranges in the x and y directions.

	Facies	Proportion	Mean	Std. dev	Variogram type	λ_x (m)	λ_y (m)	sill
ln$K$ (m/d)	Channel	0.35	3.5	0.9	spherical	20	20	1
	Non-channel	0.65	-2.5	0.6	spherical	20	20	0.4
Porosity (-)	Channel	0.35	0.15	0.04	spherical	40	40	1
	Non-channel	0.65	0.42	0.08	spherical	40	40	1

Table 2. Definition of scenarios. State variables assimilated in each scenario.

Scenario	S1	S2	S3	S4	S5	S6	S7
ln$K$	√	√	√	√	√	√	√
Porosity	√	√	√	√	√	√	√
Piezometric head	√	√	√	√			
Concentration		√		√	√		√
Temperature			√	√		√	√